This is the Pre-Published Version.
C. He, Y. Liu, X. Huang, S. Wan, Q. Chen, J. Sun, T. Zhao (2024) *A transient multi-path decentralized resistance-capacity network model for prismatic lithium-ion batteries based on genetic algorithm optimization*, **Energy Conversion and Management**, 300, 117894. doi: 10.1016/j.enconman.2023.117894

A transient multi-path decentralized resistance-capacity network model for prismatic lithium-ion batteries based on genetic algorithm optimization

C.X. He[a], Y.H. Liu[b], X.Y. Huang[b], S.B. Wan[a], Q. Chen[a], J. Sun[a,c,*], T.S. Zhao[a,c*]

[a] Department of Mechanical and Aerospace Engineering, The Hong Kong University of Science and Technology, Clear Water Bay, Kowloon, Hong Kong SAR, China

[b] Department of Building Environment and Energy Engineering, The Hong Kong Polytechnic University, Hung Hom, Kowloon, Hong Kong SAR, China

[c] Department of Mechanical and Energy Engineering, Southern University of Science and Technology, Shenzhen, 518055, China

Abstract

Battery thermal management is crucial for preventing the safety issues of lithium-ion batteries. Due to the simple modeling and fast calculation speed, the thermal resistance-capacity (RC) network model is broadly applied in the design of battery thermal management systems. However, the current simplification of heat flow paths and the lumped definition of thermal capacity causes large errors in the temperature prediction, which cannot precisely reflect the actual thermal response in complex and diverse heat transfer situations. To improve the prediction accuracy, a decentralized centroid multi-path RC network model is constructed for a typical prismatic lithium-ion battery. In the improved model, a more reasonable multiple heat flow path with additional thermal resistances is included and validated by external heating experiments, while the lumped heat capacity is legitimately discretized to other surface center points to simulate the transient temperature response precisely. In addition, the genetic algorithm is employed to determine the unknown thermal resistances and heat capacities at the attribute nodes through repeated genetic screening. Result shows that compared to the traditional RC network model, the decentralized centroid multi-path RC network model could greatly reduce the temperature prediction error from 4.240 to 0.945 ℃. This model construction method with significantly improved accuracy can also be effectively applied to batteries with other types and materials, which provides essential guidance for the application of RC networks in the field of battery thermal management and thermal safety design.

Keywords: Lithium-ion batteries; RC networks; Thermal management; Genetic algorithm

Nomenclature		
A_{bat}	surface area of prismatic battery	m^2
c_p	specific heat at constant pressure	$J\,kg^{-1}K^{-1}$
h	convective heat transfer coefficient	$W\,m^{-2}K^{-1}$
l_{chrom}	chromosome length corresponding to the binary coded	–
m_{bat}	battery mass	kg
m_i	equivalent mass lumped in node i	kg
$p_{crossover}$	crossover probability in GA computation	–
$p_{mutation}$	mutation probability in GA computation	–
$\dot{Q}_{dis}$	heat dissipation rate	W
$\dot{Q}_{j-i}$	heat flow from node j into i	W
$\dot{Q}_{soure}$	heat generation rate	W
R_{conv}	equivalent convective thermal resistance	$K\,W^{-1}$
R_{cond}	conductive thermal resistance	$K\,W^{-1}$
R_{ji}	equivalent resistance in the resistance-capacity circuit model between node j and i	$K\,W^{-1}$
t	time	s
t_{tot}	total heating time	s
T_{bat}	battery temperature	K
T_i	temperature at node i	K
T_j	temperature at node j	K
T_f	ambient temperature	K
T_{RMSE}	root-mean-square deviation of the temperature	K
$\boldsymbol{X}$	input data matrix	–
$\boldsymbol{X_n}$	input data of individual vector in $\boldsymbol{X}$	–
Y	fitness value Y corresponding to input vector $\boldsymbol{X_n}$	K

Greek symbol

λ	thermal conductivity	$W\,m^{-1}K^{-1}$

Subscripts and superscripts

bat	battery
$cond$	conductive
$conv$	convective
ct	connector
tp	positive tab
tn	negative tab
tot	total

Acronyms

BTMS	battery thermal management system
CTC	cell-to-chassis
CFD	computational fluid dynamics
FEM	finite element method
MDRC	multi-path decentralized resistance-capacity
NCM	lithium nickel manganese cobalt oxides
PCM	phase change material
PID	proportional–integral–derivative
RC	resistance-capacity
TR	thermal runaway

1. Introduction

Lithium-ion batteries have recently emerged as a typical and standard power source for electric vehicles due to their low cost, high energy density, high efficiency, and long cycle life in recent years [1,2]. However, the safety issue of lithium-ion batteries currently is one of the most critical ones that should be well addressed, necessitating a precise thermal management system (BTMS) to detect and control the temperature state of the batteries [3–7]. Typically, numerical modeling is a simple and cost-effective method to design BTMS, because an accurate heat transfer model reduces the complexity and cost of heat dissipation system and safety design [8,9].

The modeling methods of the battery module and pack-level heat transfer process primarily consist of the finite element method (FEM) and the equivalent thermal resistance-capacity (RC) network model [10–12]. The former one can predict the temperature response of the battery at any locations discretized in the model with high precision, which has been extensively studied in many BTMS designs, especially systems involving complex geometries and heat transfer processes [13–15]. For example, Mansir et al. [16] systematically investigated the temperature distribution for a small cylindrical battery module with fin structure and saturated with phase change material (PCM) through COMSOL software. Atieh Alihosseini and Maziar Shafaee [17] combined a one-dimensional (1D) battery heat generation model with a three-dimensional (3D) flow and heat transfer model to investigate the performance of the heat pipe in the thermal management system to maintain a more stable temperature condition. Xin et al. [18] compared the heat dissipation effect of air and liquid cooling thermal management methods on a cylindrical battery module and achieved a good balance of cooling performance, power consumption and lightweight. The FEM modeling method can precisely characterize the heat transfer process and determine the temperature gradient of each single cell when dealing with complex phase change, flow, and heat transfer coupling problems, which has also seen effective application in the safety prevention works e.g., the modeling of thermal runaway (TR) propagation. Li et al. [19] investigated the impact of side plates on the thermal runaway propagation based on FEM, the parameters of side plates in a battery module were optimized to mitigate thermal runaway propagation. Jin et al. [20] conducted a structural configuration on the battery arrangement for cell-to-chassis (CTC) technology by building a validated 3D FEM model. Using similar modeling techniques, their group also studied the heating power and investigated the energy flow regulations on the thermal runaway propagation characteristics of a small prismatic battery module. These FEM-based modeling research methods provide important guidance for module-level BTMS design and thermal runaway prediction. Although the FEM model can provide temperature distribution of all discrete points, the simulation result we are concerned about is primarily the temperature of only several indicative points in many cases. Especially when dealing with large-scale BTMS and safety design with complex structures that require a huge number of grids, FEM consumes high modeling costs and enormous computational resources [13]. In contrast, the RC network

model is a better option in onboard BTMS and online prediction of thermal runaway propagation with fast calculation speed and low modeling cost, in which the research object is equivalent to the corresponding electrical parts [21–23].

In recent years, the RC network model has been widely used in many fields, including battery thermal management and thermal safety issues, since it is less complex than FEM numerical model [11,24,25]. However, the trade-off for its approximation approach also sacrifices the precision of the RC network model. To address this issue, numerous improvements and refinements have been made to enhance the simulation accuracy, allowing for more reliable and accurate simulations of complex systems and phenomena. Zhu et al. [26] developed a more precise RC network model with a detailed breakdown of the thermal resistances to investigate the thermal performance of the cylindrical battery module from both axial and radial thermal directions. Xu et al. [27] developed a transient prismatic battery thermal model to provide a battery real-time temperature response in a wide temperature range of -5~55 ℃. Their model more precisely divides the battery's heat capacity into electrode winding bodies and the battery shell. Asiri et al. [28] conducted the transient heat transfer analysis on the battery with phase change material and connected by a u-tube containing Al_2O_3 based nanofluid. The pipe is divided into multiple small thermal resistance units, and the Crank-Nicolson differential method is employed to improve the solution accuracy of the transient equation. Chen et al. [29] constructed a 1D thermal resistance network model with four independent components including the gas thermal resistance in the thickness direction of a single battery. Jiang et al. [11] built a fast RC network model through a four-step prediction method for pack-level thermal runaway propagation. In their work, TR propagation features are discussed thoroughly with different TR trigger locations. The impact of PCM on TR behaviors is investigated as well. In the above studies, the thermal resistance network model fully embodies its advantages of high calculation speed and simplicity in model construction. To improve the versatility of RC model, Wang et al. [30] investigated the ejection and spread behavior of venting gases through a validated CFD model and constructed the RC network to calculate the complex module-level heat transfer process during battery TR propagation. The advantages of both models can be highlighted by connecting FEM and RC network models simultaneously. However, the accuracy of the RC network model is still greatly affected by the division methods of the thermal resistance. The traditional RC network model has a clear geometric structure for the division of the research object, which is only suitable for solving problems with simple heat transfer paths. In cases with complex and diverse heat transfer paths, the actual heat transfer process can hardly be depicted. Besides, in the traditional RC network model, the entire heat capacity of the object is concentrated at the geometric center when dealing with the transient heat transfer process. Such an approximation will cause prediction errors in the temperature response of other feature points that should have included the corresponding heat capacity.

To this end, this paper developed a multi-path decentralized resistance-capacity (MDRC) network model for a typical 25Ah prismatic lithium-ion battery, of which the properties are listed in Table 1. As shown in the workflow of the model construction process (Fig. 1), a more accurate network with multiple heat flow paths and additional thermal resistances is applied to better simulate the heat transfer process. Besides, the lumped heat capacity is legitimately discretized to other surface center points to precisely simulate the transient temperature response. Then, external heat experiments were conducted to build the connections between heat capacity and thermal resistances for each node. A genetic algorithm is used to solve the unknown thermal resistances and decentralized heat capacities. Through repeated genetic screening, the error between the predicted and the measured temperature is gradually reduced and reaches an ultra-low level, representing the high accuracy of the newly built model.

Table 1. Properties of the 25Ah NCM prismatic Battery [31].

Specification	Value
Mass	0.789 kg
Specific heat capacity	1100 J $kg^{-1}K^{-1}$
Rated capacity	25 Ah
Battery length	148 mm
Battery width	26.5 mm
Battery height (except the tab)	91 mm
Tab length	33.5 mm
Tab width	20.5 mm
Tab height	5 mm
Thermal conductivity in x direction	21 W m^{-1} K^{-1}
Thermal conductivity in y direction	1.1 W m^{-1} K^{-1}
Thermal conductivity in z direction	21 W m^{-1} K^{-1}

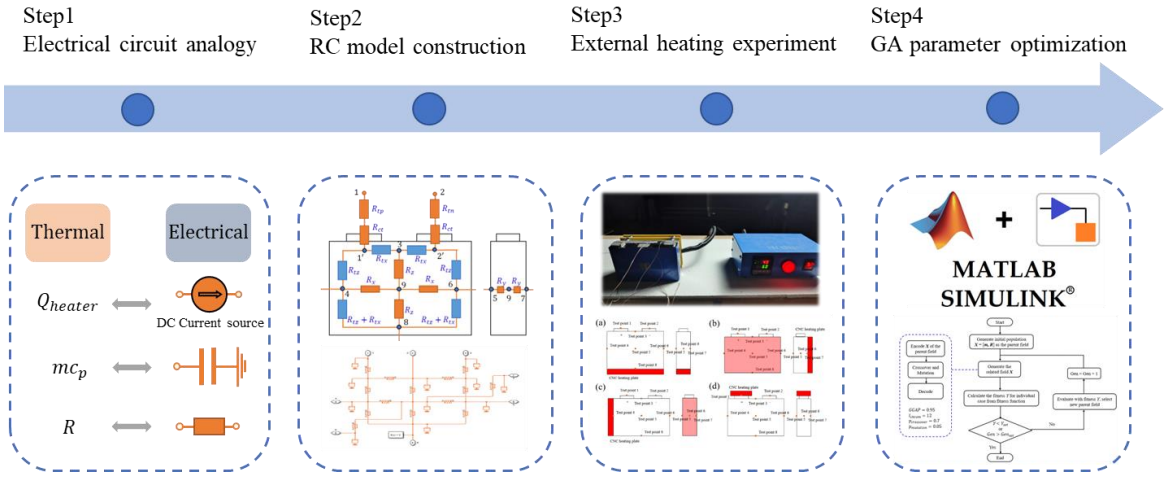

Fig. 1. Schematic diagram of the MDRC network model construction process.

2. Model construction

2.1 Thermal resistance-capacitance network model development

Fig. 2 depicts the development process of the RC network model. To clearly indicate the relationship between the internal thermal resistances of the battery, the heat source term as well as the convective heat transfer thermal resistance between each surface and the environment is not depicted in the schematic diagram. Nine representative points (1', 2', 3, 4, 5, 6, 7, 8, 9) located at the center of corresponding surface were chosen as nodes in RC network, as shown in Fig. 2a. Node $1'$ and $2'$ are located on the upper surface of the prismatic battery core, directly below the center of the positive and negative electrodes (node 1 and 2), respectively.

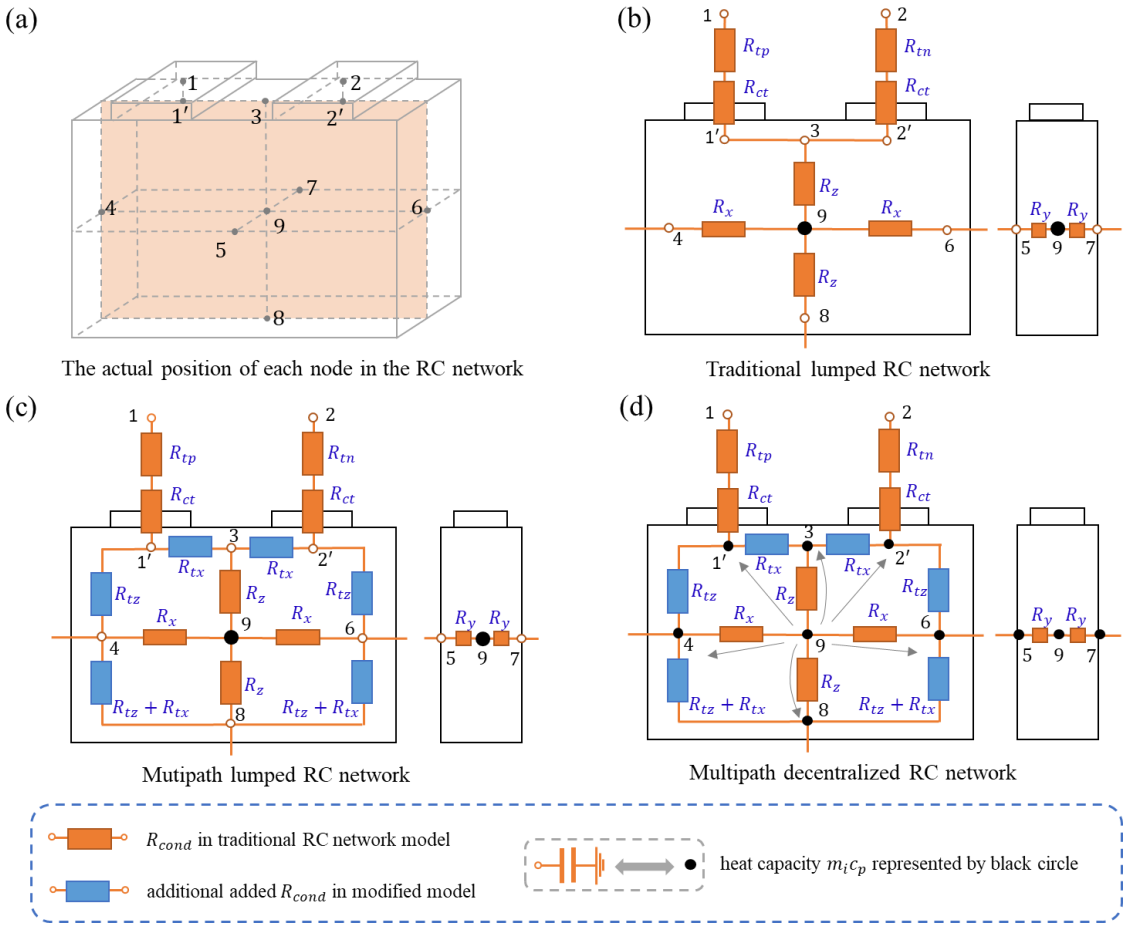

Fig. 2. Schematic diagrams of (a) traditional lumped RC network model, (b) multi-path lumped RC network model, and (c) MDRC network model.

It can be seen that in a traditional RC network (Fig. 2b), the heat should flow through the geometric center of the battery (node 9) from one surface node to another because there is no direct thermal resistance connection between the surface nodes ($1'$, $2'$, 3, 4, 5, 6, 7, and 8). As an modification, the multi-path lumped RC network (Fig. 2c) adds extra thermal resistances between each feature point to the conventional RC network. Besides, the thermal resistance between node $1'$ and $2'$ are also included

to evaluate the uneven temperature distribution on the top side of the battery. To make the model more accurate, instead of simply concentrating the mass in the geometric center of the battery, the mass is discretized to the other 8 test points ($1'$, $2'$, 3, 4, 5, 6, 7, and 8) to reduce the heat capacity at the center point while increasing the weight of other attributed nodes with the total mass unchanged, named as the MDRC network model (Fig. 2d).

The conductive thermal resistances of the traditional RC model can be calculated by,

$$R_{cond} = \frac{\Delta x}{A \cdot \lambda_{bat}} \tag{1}$$

where R_{cond} is the absolute conductive thermal resistance (K W^{-1}) across the thickness of the sample. Δx is the thickness of the sample measured on a path of the heat flow. A is the cross area perpendicular to the path of heat flow. λ_{bat} is the thermal conductivity of the sample. Once the geometric parameters and thermal conductivity are known, the resistance of each sample is determined. R_{ct} represents the contact resistance between the tab and the battery core, which is mainly contributed by the air gap at the top of the battery and the connection between the current collector and the tab. All the thermal resistances of the 25 Ah prismatic battery in the traditional lumped RC network model are listed in Table 2.

Table 2. Determination of the thermal resistances of the traditional lumped RC network model.

Specification	Value
R_{tp}	0.046 K W^{-1}
R_{tn}	0.050 K W^{-1}
R_{ct}	2.150 K W^{-1}
R_x	1.46 K W^{-1}
R_y	0.89 K W^{-1}
R_z	0.55 K W^{-1}

The thermal resistance of the equivalent convection thermal resistance is written as,

$$R_{conv} = \frac{1}{A_{conv} \cdot h_{conv}} \tag{2}$$

where A_{conv} is the convection heat transfer area. h_{conv} is the equivalent convection heat transfer coefficient, which is about 3.2 W m^{-2} K^{-1}. Each thermal resistance in the traditional lumped RC network model has been calculated and set in the Simulink program in the Supplementary Information. It can be seen from Fig. 2b that, when a certain surface of the battery is heated (e.g., node 1), the heat must first flow through the geometric center of the battery (node 9) to reach the center of other surfaces (e.g., node 4), which is also an inappropriate approximation since the heat will flow directly from one surface to the center of the other faces. In addition, the center points at the root of the tabs (node $1'$and $2'$) are

directly connected to the center of the top surface of the battery (node 3) without any thermal resistances [11]. As a result, the temperature of point 1′, 2′, and 3 calculated by the traditional RC network model are always the same, which cannot accurately reflect the actual temperature distribution. To reflect the actual heat flow process, multi-path lumped RC network model is constructed, seen in Fig. 2c, in which all newly added thermal resistances are indicated by blue rectangles. The thermal resistance R_{tx} and R_{tz} are arranged between the center points of the adjacent surfaces (e.g., R_{tx} between node 1′ and 3, R_{tz} between node 1′ and 4), which provides the path for heat to flow directly between the two adjacent faces. The prismatic battery is basically symmetrical in the vertical direction, so the thermal resistance between the center of the side surface (node 4 and node 6) and the center of the bottom surface (node 8) is equal to $(R_{tx} + R_{tz})$. Nevertheless, the concentration of the heat capacity at the center is still not practically precise, which results in an inaccurate temperature response of other locations during the transient heating process. The temperature rise rate at the nodes close to the heat source is faster than the actual rate, and that of the point away from the heating surface is slower than the actual rate since the heat needs to first flow into the lumped heat capacity of the geometric center. This phenomenon can be clearly observed in section 4.2. To better reduce the thermal response error caused by the simplification in the lumped model, the lumped mass is decentralized to each feature point, and is called as MDRC network model shown in Fig. 6c.

2.2 Governing equations of the resistance-capacitance network model

The corresponding energy balance equation for each node i in the MDRC network model is,

$$m_i c_p \frac{dT_i}{dt} = \dot{Q}_{source} + \Sigma \dot{Q}_{k-i} \tag{3}$$

where m_i is the equivalent mass lumped in node i. c_p is the specific heat capacity of the battery. $\dot{Q}_{source}$ represents all self-heating heat generation power at point i, which could be the heat generation through charge/discharge process or the heat generation through the TR process. $\Sigma \dot{Q}_{k-i}$ is the sum of all heat flow into and out of the node *i*. The heat flow between node j and i can be written as,

$$Q_{j-i} = \frac{T_j - T_i}{R_{ji}} \tag{4}$$

where T_j and T_i is the temperature of node j and i, respectively. R_{ji} is the thermal resistance between node j and i. The heat dissipated from the convection heat transfer process is given as,

$$\dot{Q}_{dis} = \frac{T_f - T_i}{R_{conv}} \tag{5}$$

where T_f is the ambient temperature. R_{conv} can be calculated by Eq. (2).

The temperature at the center of the battery surface contact with the heater (node *n*) is measured by a thermocouple, as the temperature boundary condition of the simulation model.

$$T_n = T_{heater} \tag{6}$$

2.3 Parameter solving through genetic algorithm

The additional thermal resistances between each feature point and the decentralized heat capacitance in the MDRC network model can improve the simulation accuracy compared to the traditional RC network model. However, the values of these thermal resistances and the decentralized mass can no longer be calculated according to the geometric structures. Therefore, intelligent optimization algorithms are applied to identify the unknown parameters of these models based on external heating experiments. Fig. 3 presents the flow chart of the parameter calculation and optimization process. The whole iterative calculation program is completed by MATLAB and Simulink.

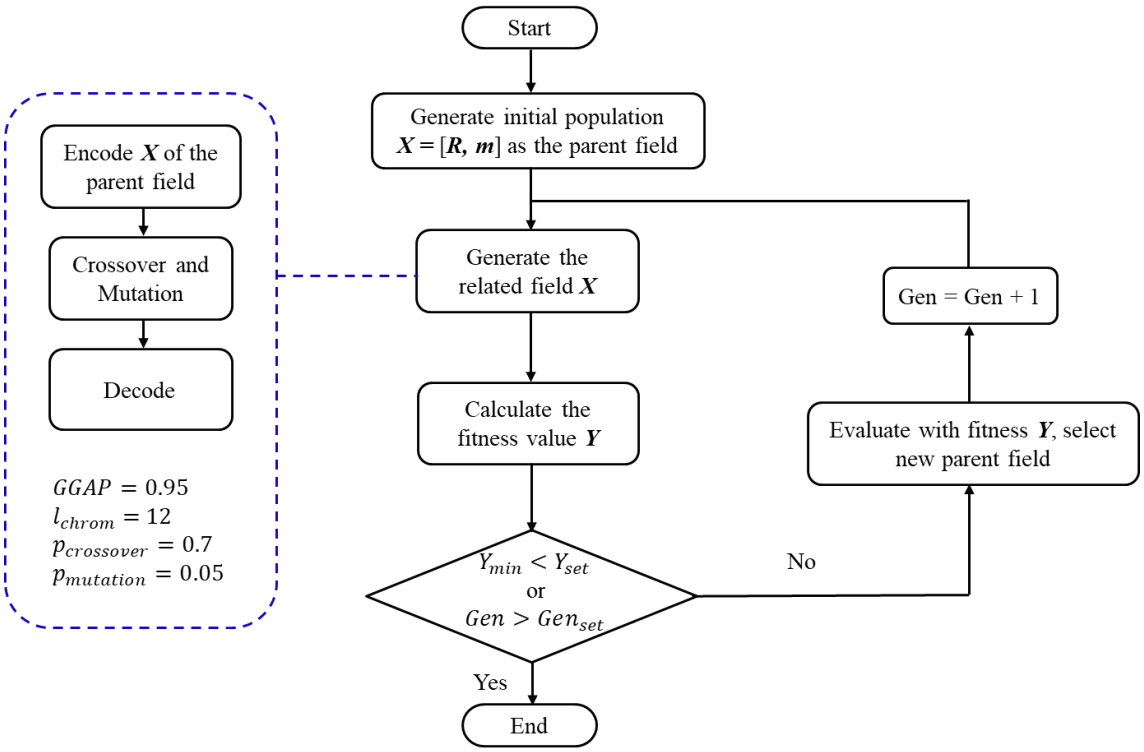

Fig. 3. Flowchart of the genetic algorithm of the MDRC network model.

In each generation, the input data matrix $\boldsymbol{X}$ includes the mass of each node and every thermal resistance in the MDRC network model. Each vector $\boldsymbol{X_n}$ in $\boldsymbol{X}$ includes 12 variables, which can be written as,

$$\boldsymbol{X_n} = [R_{ct}, R_{tx}, R_{tz}, R_x, R_y, R_z, m_1, m_3, m_4, m_5, m_8, m_9] \tag{10}$$

where n represents the population size, or the number of individuals in each generation. R_{tp} and R_{tn} are respectively 0.046 and 0.050 K W^{-1} determined in the traditional model part. R_{ct} is the contact thermal resistance between the tabs and the electrodes. Not all the mass variables are included in the input data because $m_1 = m_2$, $m_4 = m_6$, and $m_5 = m_7$. The constraint condition of the battery mass of each point is,

$$m_{bat} = m_1 + m_2 + \cdots + m_9 \tag{11}$$

After the input vector $\boldsymbol{X_n}$ is given, the temperature response to the bottom, front, side, and tab heating experiments could be acquired through the MDRC network model. For each external heating

experiment k (k = 1, 2, 3, 4 represents bottom, front, side, and tab heating experiment, respectively), the root-mean-square deviation of the temperature of each node i (i = 1, 2, …, 8) is calculated as,

$$T_{RMSE,i,k} = \sqrt{\frac{\Sigma\left[T_{i,sim}(t) - T_{i,\exp}(t)\right]^2}{t_{tot}}} \quad (t = 1, 2, \ldots, 3600\ \mathrm{s}) \tag{12}$$

where $T_{i,sim}(t)$ and $T_{i,exp}(t)$ are the temperature of point i calculated by the network model and the experimental test at time t, respectively. The temperature data collected by thermocouples updates every second. The total time of the heating experiment t_{tot} is 3600 s. The fitness value Y at each heating condition k is used to depict the entire error between the simulation and the experiment, which is defined as,

$$Y_k = \frac{\Sigma T_{RMSE,i}}{8} \ (k = 1, 2, 3, 4) \tag{13}$$

$$Y = \frac{(Y_1 + Y_2 + Y_3 + Y_4)}{4} \tag{14}$$

The smaller the fitness value Y is, the more precisethe model is, and the more reliable the input vector $\boldsymbol{X_n}$ is.

The initial parent field population (the initial input parameters) of the genetic algorithm is randomly generated with a uniform distribution within a restricted range. In the iterative process of the genetic algorithm, the population size n is set to 500. Each variable in an input vector $\boldsymbol{X_n}$ is first discretized within the limited continuous range and then binary coded. The chromosome length corresponding to the binary coded variable is set to 12 to ensure search accuracy in the optimization operation. After obtaining the input matrix $\boldsymbol{X}$, the program will calculate the fitness value Y correlating to each set of input parameters, and then use roulette wheel selection to find the parent vectors in the next genetic optimization process. The chromosomes of the selected parent generation adopt uniform crossover to generate offspring generation. The crossover probability $p_{crossover}$ of the gene locus relating to each variable is 0.7. and after the crossover, the mutation possibility $p_{mutation}$ of each gene locus equals 0.05 to improve the robustness of the calculation process. In addition, the individuals with good fitness values in the parent generation will also be selected into the next offspring, and the ratio of new individuals to the total number of individuals in each generation (defined as generation gap, GGAP) is set to 0.95. The MATLAB source code of the genetic algorithm iterative process as well as the RC network Simulink model are given in the Supplementary Information.

3. Experiment

After establishing the MDRC network model, infrared thermography and external battery heating experiment are first carried out at the Fire Engineering laboratory of The Hong Kong Polytechnic University to conduct the model validation. A 25Ah NCM prismatic battery standardized in DIN SPEC 91252 [32] proposed by VDA (Verband der Automobilindustrie) is investigated in the heating experiment. The battery was first charged by constant current (1C)-constant voltage (4.2 V with 1/20 C

cut-off current) and discharged to 2.7 V by constant current (1C) at 25 °C for 10 cycles prior to the heating test. The digitally controlled heater is designed to have the same shape as the battery contact surface to completely cover the heating surface. The heater will first heat up to the set temperature (60 °C) during operation, and then maintain a constant temperature through a proportional–integral–derivative (PID) control method. Silica gel is coated on the contact surface between the battery and the heater to reduce the contact thermal resistance.

3.1 Tab heating infrared thermography

Tab heating infrared thermography experiment is conducted to intuitively estimate the temperature distribution of the battery when the tabs are heated locally, because battery tabs are electrically connected by bus bar, which is an essential heat flow path in the thermal diffusion process of a battery module. The tab heating experiment setup is demonstrated in Fig. 4. The battery is arranged on a 10 mm thick thermal insulation pad to prevent heat conduction between battery and the desk. The FLIR A700 camera is arranged in front of the battery heating setup. No thermocouple sensors are attached to the battery to prevent obscuring the thermal infrared pictures during the tab heating thermography process.

Fig. 4. Tab heating infrared thermography experimental setup.

Fig. 5 shows the large surface temperature distribution of the prismatic battery under tab heating conditions. The maximum temperature of the color bar is set at 40 °C to depict the temperature gradient clearly. A noticeable temperature gradient between the positive and negative tabs of the battery can be seen in the large surface thermography. The temperature difference at t = 720 s could reach over 30 °C. However, such a large temperature difference could not be evaluated through traditional lumped RC network model since no thermal resistance is included between two tabs. In addition, the isotherm of the battery large surface is a nearly straight line, indicating that the temperature at the midpoint of the left side is almost equal to the temperature at the midpoint of the top side (as verified by the external heating test). The regulation of such thermal response cannot be predicted either because the heat

coming from the tab node in the traditional RC network model must first flow into the geometric center node of the battery before flowing into the node of the side surface, which is inaccurate in practice. This experiment comprehensively illustrates the limitations of the traditional RC network and the necessity of including multi-path thermal resistances in the model.

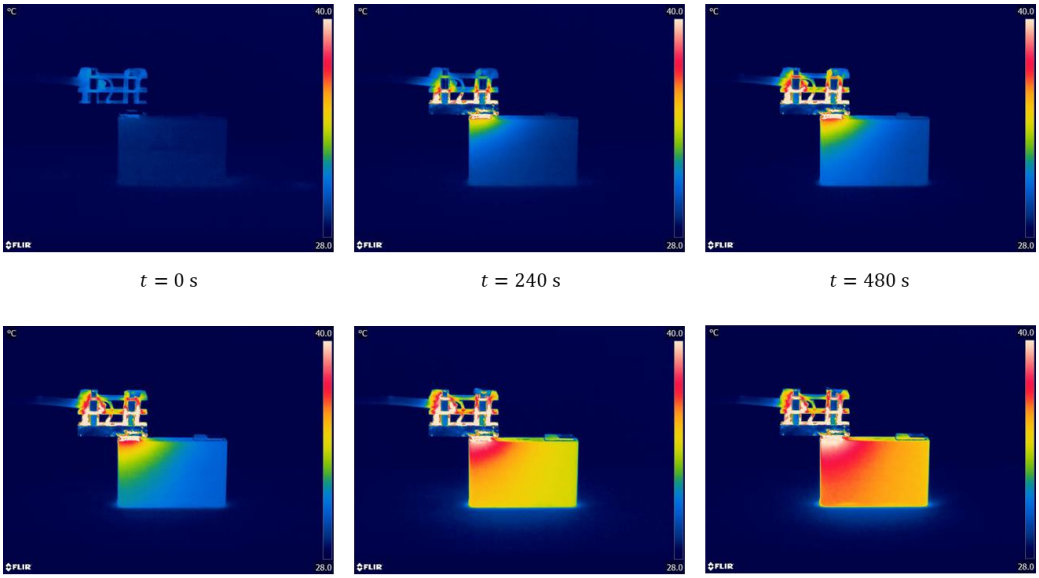

Fig. 5. Temperature distribution of the battery large surface under tab heating condition.

3.2 External heating experiment

External heating experiments from four different directions are conducted for model validation, in which the temperature data calculated by each RC network model will be compared to the experimental result to evaluate the simulation accuracy. In addition, the convection heat transfer coefficient as well as the temperature boundary conditions of the heating surface are determined, which are fundamental settings of the simulation. Fig. 6 shows the experimental setup of the external heating test. To reduce the heat transfer from forced convection and radiation, the battery and heater are wrapped in thermal insulation cotton, the outside of which is pasted by aluminum foil with low radiation absorption coefficient. The heating surfaces include the bottom surface, the front surface, the side surface, and the positive tab of the battery, respectively. 8 K-type thermocouples with 0.1°C uncertainty are attached to the center of each battery surface, as shown in Fig. 7. The red square represents the PID controlled heaters. Each external heating experiment lasts over 2 hours to ensure that the battery temperature is stabilized. The temperature data at the heating interface is applied as the temperature boundary condition of the simulation model. After heating, the equivalent convective heat transfer coefficient of the battery could be calculated from the natural cooling process, which is about 3.2 W m^{-2} K^{-1}. The experimental data records and the specific calculation process of the natural convective heat transfer coefficient can be found in the Supplementary Information.

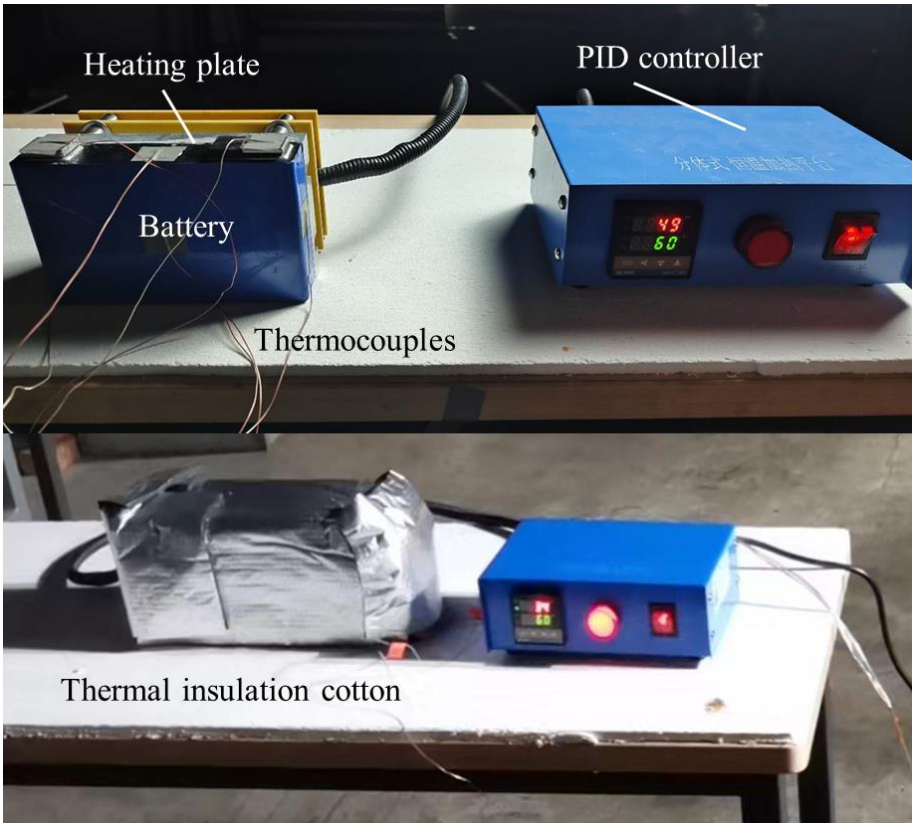

Fig. 6. External heating experimental setup.

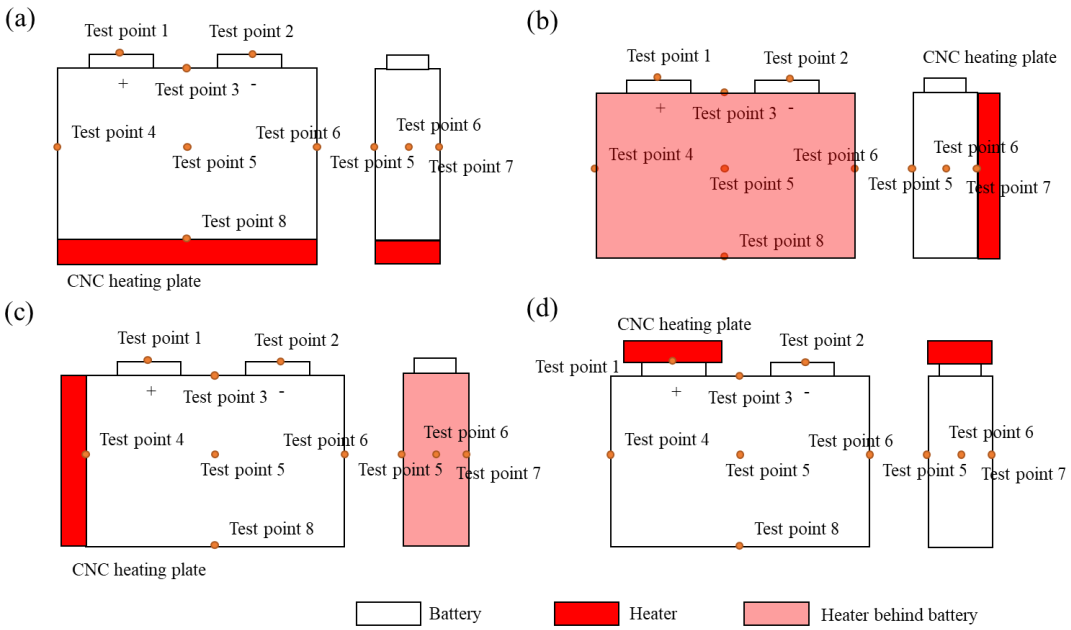

Fig. 7. Schematic diagram of the external heating experiment.

4. Result and discussion

4.1 Genetic algorithm convergence process

Fig. 8 shows the simulation accuracy of the MDRC model with the generation number of the genetic algorithm. A significant evolution trend is revealed in the population from the 1st to the 50th generation. It is seen that when the genetic algebra reaches 10, the results are relatively stable, at which time the minimum fitness value Y_{min} has dropped under 1 °C. As the generation number continues increasing from 10th to 50th, the average fitness values Y_{avg} fluctuates within 0.969 to 0.945 °C, of which the volatility is no more than 0.02 °C, indicating that the genetic algorithm has basically converged. In the 50th generation, the lowest fitness result Y_{min} equals 0.945 °C, which is a sufficiently low prediction value indicating that the model can effectively forecast the temperature variation trend of each point of the battery across four different external heating experiments.

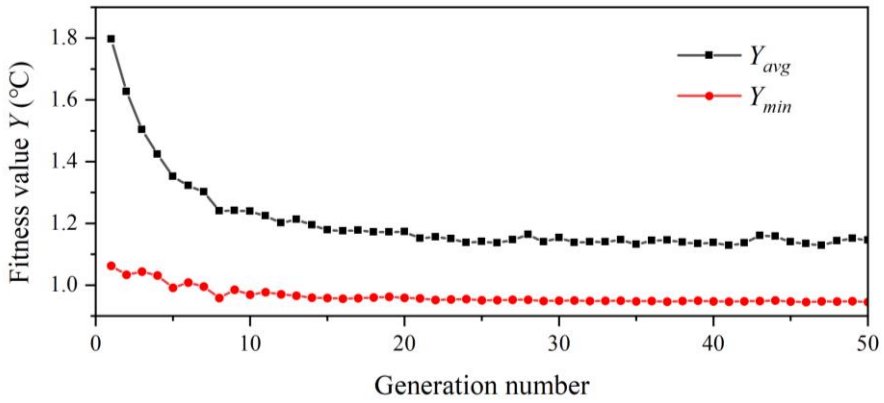

Fig. 8. Convergence curve of the genetic algorithm generation number by reporting the best fitness and average fitness of the population from the 1st to the 50th generation

Fig. 9 indicates the relationship between each thermal resistance group and the fitness value Y in the 1st, 5th, and 50th generations of the genetic algorithm. In the first generation, the value of each thermal resistance is relatively evenly distributed within the initial range, whereas the corresponding fitness value Y is disorderly distributed between 1-3.5 °C, with the average fitness result Y_{min} reaching as high as 1.8 °C. The scattered points move downward as the genetic algebra increases. For each resistance variable, the blue scatter points are obviously concentrated to a specific thermal resistance value when the genetic generation reaches 50 generations, and the average fitness value Y_{min} is also reduced to 1.2 °C. The scatter diagram also shows that R_{tx} is about 3.6 times the thermal resistance R_x, indicating that the extra horizontal path added in the MDRC model still bears a significant portion of the heat flow. However, R_{tz} is 12.5 times the thermal resistance R_z, revealing that in the vertical direction, the primary heat flow path is still to reach the center of the battery first (point 9), and then from the center to the two sides of the battery (point 4 and 6).

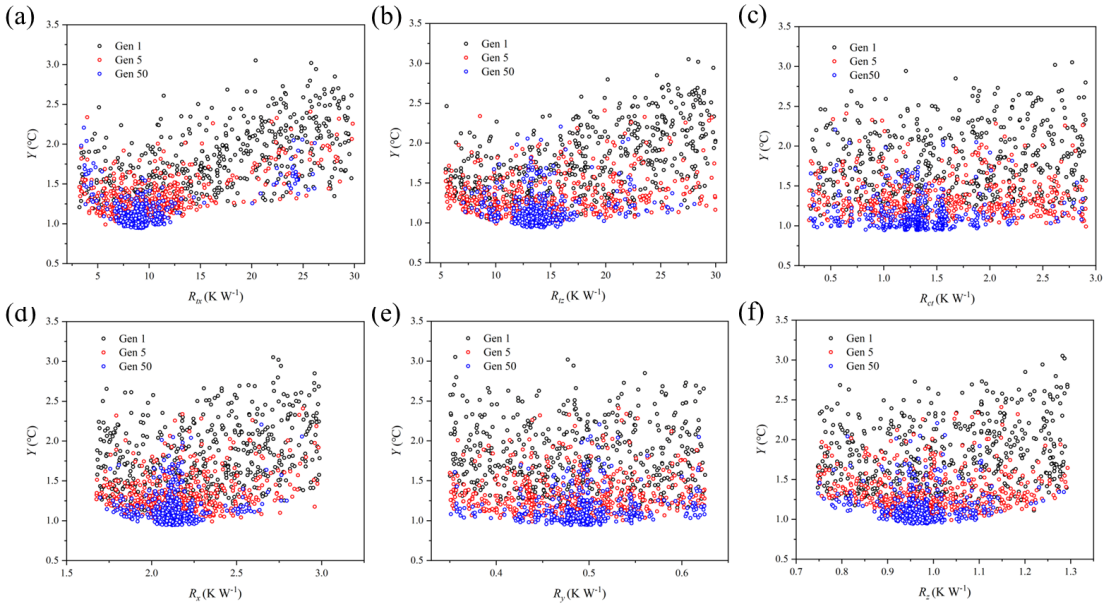

Fig. 9. Distribution of input thermal resistance in 1st, 5th and 50th genetic algorithm calculation process

It can be seen from Fig. 10 that the population gradually moves towards the south of the distribution map to produce lower temperature prediction error. In addition, as the optimization generation updates from 1st to 50th, the heat capacity proportional to the equivalent mass of the MDRC network model is generally concentrated on the center of the large surface of the battery, while the mass of other feature points accounts for only 10.5% in sum. This is because the current multi-path decentralized RC model neglects the heat transfer path directly from the center of the large surface of the battery to the center of other surfaces. The heat that should have traveled through these paths all passes through R_y to the battery center (point 9) and then transfers to the center of other surfaces. As a result, the heat flow into these places must first pass through the center of the battery to raise the temperature of the entire battery, of which the heat capacity corresponds to the total lumped mass. Therefore, when the mass is completely concentrated at the battery center, the temperature of those points away from the heater calculated by the multi-path lumped RC network model will be lower than the experimental results after the same heating period, especially under the front heating condition. In contrast, distributing the mass to the center points of the battery's large surfaces could effectively reduce the delay effect of the lumped mass simplification. Thus, after the mass is redistributed to the other feature points including the front and rear surfaces, the temperature rise rate at these positions is effectively increased. It is worth noting that the mass range of the initial input has been pre-optimized by the genetic algorithm, and the specific program and documents of each generation is given in Supplementary Information. The best case among the 50 generations is determined as the input parameter of the MDRC model, which is listed in Table 3.

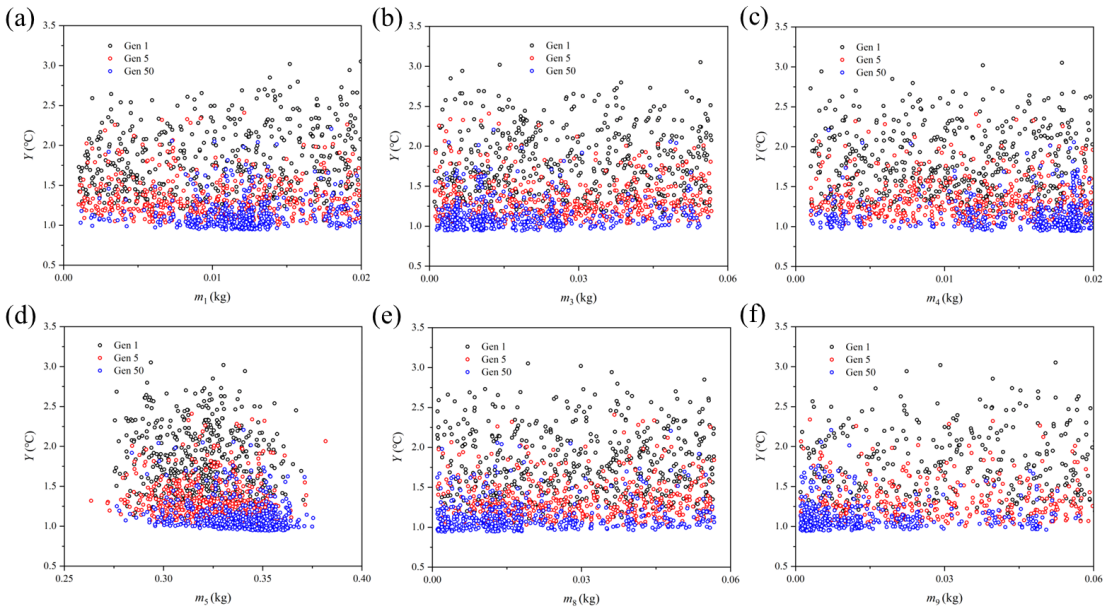

Fig. 10. Distribution of input mass in 1st, 5th and 50th genetic algorithm calculation process

Table 3. Determined input parameter of the final MDRC model.

Specification	Value
R_{ct}	1.007 K W^{-1}
R_{tx}	9.241 K W^{-1}
R_{tz}	14.36 K W^{-1}
R_x	2.120 K W^{-1}
R_y	0.4803 K W^{-1}
R_z	0.9058 K W^{-1}
m_1	0.0109 kg
m_3	0.0186 kg
m_4	0.0188 kg
m_5	0.3532 kg
m_8	0.0025 kg
m_9	0.0021 kg

4.2 Model validation and comparison

Fig. 11 compares the simulation accuracy of the traditional RC model, multi-path lumped RC model and MDRC model under bottom heating and front heating conditions. To make the comparison results more intuitive, only several representative test points are compared with the experimental data. As can be seen, the traditional RC model is unable to distinguish temperature differences between different test

points. Except for the directly heated points, the maximum temperature difference between other measuring points is less than 0.2 °C (in the experiment, the maximum temperature difference reaches over 5 °C). Temperature differences can be reflected by the multi-path lumped RC model. The multi-path lumped RC model can reflect the temperature variations to some extent. For example, in the bottom heating condition, the temperature at the center of the large surface of the battery (point 5) rises faster than that at the tab point away from the bottom surface (point 1). However, since the thermal resistance is not optimized in the thickness direction of the battery, the simulation results are unable to display the temperature variation in the case of front heating. By contrast, the T_{RMSE} the MDRC model within 1800 s does not exceed 0.5 °C, which agrees well with the experimental data under both localized heating conditions.

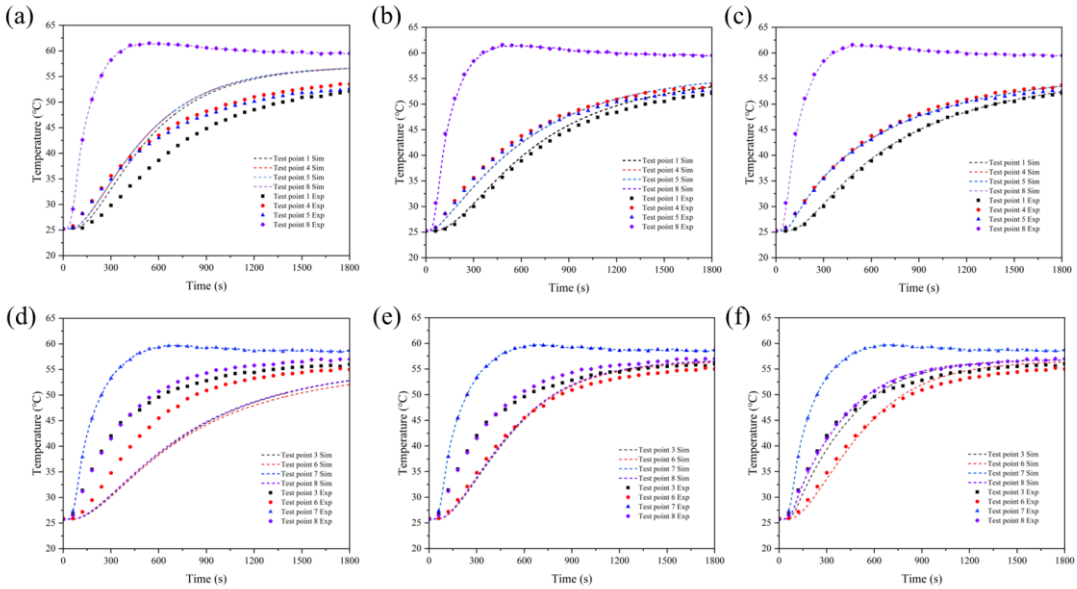

Fig. 11. Comparison of the accuracy of different RC model under (a-c) bottom heating and (d-f) front heating conditions

Fig. 12 evaluates the prediction accuracy of the classic RC model, multi-path lumped RC model, and MDRC model under bottom heating and front heating conditions. The same as bottom heating and front heating conditions, traditional RC models cannot reflect temperature differences between different locations of the battery. Multi-path lumped RC model and MDRC model can both produce improved prediction outcomes. Under side heating condition, the temperature of the upper center of the battery (point 3), rise more quickly in the MDRC model than in multi-path lumped RC, which is closer to the experimental data. This is due to the fact that the total battery mass of the multi-path lumped RC model is concentrated in its center node. This rough approximation makes the temperature of other test points that are indirectly heated by the battery center point rise slower than in the real case. In addition, it can be seen that under side heating condition, the temperature rise rate at each point of the battery is slow,

and both two multi-path RC models perform well.

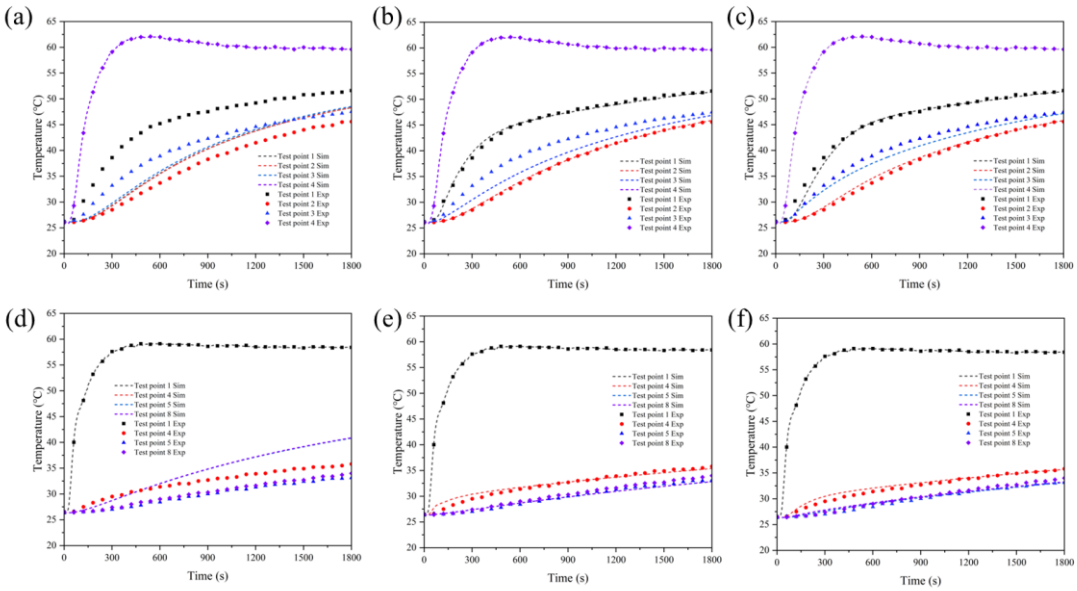

Fig. 12. Comparison of the accuracy of different RC model under (a-c) side heating and (d-f) tab heating conditions

Conclusion

In this study, the temperature variation regulation of the NCM prismatic battery is investigated under different local heating conditions. On this basis, the MDRC is proposed by including multi-path thermal resistances and distributing mass to each selected node of the conventional RC network model. The physical parameters of the newly developed model are identified through a uniformly crossed genetic algorithm. The performance of the classic RC model, multi-path lumped RC model, and MDRC model is carefully compared under different local heating conditions. The findings demonstrate that the optimized MDRC model can effectively improve the precision of the transient temperature response prediction of the prismatic battery. The specific conclusions are as follows:

(1) Despite the poor thermal conductivity in the thickness direction of the prismatic battery, the thermal resistance in the thickness direction is the smallest due to the large contact area of the large surface, followed by the length direction, and the height direction is the largest. Therefore, cooling/heating through the large surface is still the most effective battery thermal management strategy.

(2) The efficiency of heat transfer through the connection of the tabs is lower than that of the rest of the main surface contact heat exchange. However, there is still a significant temperature difference between the two tabs of the battery, which cannot be identified through the classic RC model and needs to be obtained by adding multi-path resistances.

(3) The multi-path lumped RC model and MDRC model optimized by the genetic algorithm can

more accurately represent the temperature response of the battery under various heating conditions, and the transient temperature response of the decentralized RC model is more accurate, of which the average T_{RMSE} is maintained within 0.945 °C.

(4) In the case of ignoring the multi-path thermal resistance in the thickness direction, the mass of the transient RC model is mainly concentrated in the center (90%) of the front and back surfaces of the battery. Therefore, within the allowable range of error, the center of mass of the battery can be approximately placed on the front and rear surfaces to simplify the computation.

Acknowledgement

The work described in this paper was fully supported by a grant from the Research Grant Council of the Hong Kong Special Administrative Region, China (Project No. 16204921).

Reference

[1] H. Niu, C. Chen, Y. Liu, L. Li, Z. Li, D. Ji, X. Huang, Mitigating thermal runaway propagation of NCM 811 prismatic batteries via hollow glass microspheres plates, Process Safety and Environmental Protection. 162 (2022) 672–683. https://doi.org/10.1016/j.psep.2022.04.049.

[2] Y. Liu, H. Niu, C. Xu, X. Huang, Thermal runaway propagation in linear battery module under low atmospheric pressure, Applied Thermal Engineering. 216 (2022) 119086. https://doi.org/10.1016/j.applthermaleng.2022.119086.

[3] P. Qin, J. Sun, X. Yang, Q. Wang, Battery thermal management system based on the forced-air convection: A review, ETransportation. 7 (2021) 100097. https://doi.org/10.1016/j.etran.2020.100097.

[4] M. Shahjalal, T. Shams, Md.E. Islam, W. Alam, M. Modak, S.B. Hossain, V. Ramadesigan, Md.R. Ahmed, H. Ahmed, A. Iqbal, A review of thermal management for Li-ion batteries: Prospects, challenges, and issues, Journal of Energy Storage. 39 (2021) 102518. https://doi.org/10.1016/j.est.2021.102518.

[5] Q.L. Yue, C.X. He, M.C. Wu, T.S. Zhao, Advances in thermal management systems for next-generation power batteries, International Journal of Heat and Mass Transfer. 181 (2021) 121853. https://doi.org/10.1016/j.ijheatmasstransfer.2021.121853.

[6] M.W. Nazar, N. Iqbal, M. Ali, H. Nazir, M.Z.B. Amjad, Thermal management of Li-ion battery by using active and passive cooling method, Journal of Energy Storage. 61 (2023) 106800. https://doi.org/10.1016/j.est.2023.106800.

[7] S. Wang, D. Zhang, C. Li, J. Wang, J. Zhang, Y. Cheng, W. Mei, S. Cheng, P. Qin, Q. Duan, J. Sun, Q. Wang, Numerical optimization for a phase change material based lithium-ion battery thermal management system, Applied Thermal Engineering. 222 (2023) 119839. https://doi.org/10.1016/j.applthermaleng.2022.119839.

[8] K. Shen, J. Sun, Y. Zheng, C. Xu, H. Wang, S. Wang, S. Chen, X. Feng, A comprehensive analysis and experimental investigation for the thermal management of cell-to-pack battery system, Applied Thermal Engineering. 211 (2022) 118422. https://doi.org/10.1016/j.applthermaleng.2022.118422.

[9] P. He, H. Lu, Y. Fan, H. Ruan, C. Wang, Y. Zhu, Numerical investigation on a lithium-ion battery thermal management system utilizing a double-layered I-shaped channel liquid cooling plate exchanger, International Journal of Thermal Sciences. 187 (2023) 108200. https://doi.org/10.1016/j.ijthermalsci.2023.108200.

[10] Q. Yu, A. Abidi, M.Z. Mahmoud, E. Hasani Malekshah, H.Ş. Aybar, Numerical evaluation of the effect of air inlet and outlet cross-sections of a lithium-ion battery pack in an air-cooled thermal management system, Journal of Power Sources. 549 (2022) 232067. https://doi.org/10.1016/j.jpowsour.2022.232067.

[11] Z.Y. Jiang, Z.G. Qu, J.F. Zhang, Z.H. Rao, Rapid prediction method for thermal runaway propagation in battery pack based on lumped thermal resistance network and electric circuit analogy, Applied Energy. 268 (2020) 115007. https://doi.org/10.1016/j.apenergy.2020.115007.

[12] K. Smith, G.-H. Kim, E. Darcy, A. Pesaran, Thermal/electrical modeling for abuse-tolerant design of lithium ion modules, International Journal of Energy Research. 34 (2010) 204–215. https://doi.org/10.1002/er.1666.

[13] X. Feng, X. He, M. Ouyang, L. Lu, P. Wu, C. Kulp, S. Prasser, Thermal runaway propagation model for designing a safer battery pack with 25Ah LiNixCoyMnzO2 large format lithium ion battery, Applied Energy. 154 (2015) 74–91. https://doi.org/10.1016/j.apenergy.2015.04.118.

[14] K.F. Yeow, H. Teng, Characterizing Thermal Runaway of Lithium-ion Cells in a Battery System Using Finite Element Analysis Approach, SAE International Journal of Alternative Powertrains. 2 (2013) 179–186.

[15] G. Guo, B. Long, B. Cheng, S. Zhou, P. Xu, B. Cao, Three-dimensional thermal finite element modeling of lithium-ion battery in thermal abuse application, Journal of Power Sources. 195 (2010) 2393–2398. https://doi.org/10.1016/j.jpowsour.2009.10.090.

[16] I.B. Mansir, N. Sinaga, N. Farouk, M. Aljaghtham, C. Diyoke, D.D. Nguyen, Numerical simulation of dimensions and arrangement of triangular fins mounted on cylindrical lithium-ion batteries in passive thermal management, Journal of Energy Storage. 50 (2022) 104392. https://doi.org/10.1016/j.est.2022.104392.

[17] A. Alihosseini, M. Shafaee, Experimental study and numerical simulation of a Lithium-ion battery thermal management system using a heat pipe, Journal of Energy Storage. 39 (2021) 102616. https://doi.org/10.1016/j.est.2021.102616.

[18] S. Xin, C. Wang, H. Xi, Thermal management scheme and optimization of cylindrical lithium-ion battery pack based on air cooling and liquid cooling, Applied Thermal Engineering. 224 (2023) 120100. https://doi.org/10.1016/j.applthermaleng.2023.120100.

[19] K. Li, H. Wang, C. Xu, W. Wu, W. Zhang, J. Hou, X. Rui, Y. Chen, L. Fan, X. Feng, M. Ouyang, Multi-objective optimization of side plates in a large format battery module to mitigate thermal runaway propagation, International Journal of Heat and Mass Transfer. 186 (2022) 122395. https://doi.org/10.1016/j.ijheatmasstransfer.2021.122395.

[20] C. Jin, Y. Sun, J. Yao, X. Feng, X. Lai, K. Shen, H. Wang, X. Rui, C. Xu, Y. Zheng, L. Lu, H. Wang, M. Ouyang, No thermal runaway propagation optimization design of battery arrangement for cell-to-chassis technology, ETransportation. 14 (2022) 100199. https://doi.org/10.1016/j.etran.2022.100199.

[21] Robust Estimation of Battery System Temperature Distribution Under Sparse Sensing and Uncertainty | IEEE Journals & Magazine | IEEE Xplore, (n.d.). https://ieeexplore.ieee.org/document/8626763 (accessed March 31, 2023).

[22] Y. Ma, Y. Cui, H. Mou, J. Gao, H. Chen, Core temperature estimation of lithium-ion battery for EVs using Kalman filter, Applied Thermal Engineering. 168 (2020) 114816. https://doi.org/10.1016/j.applthermaleng.2019.114816.

[23] F. He, L. Ma, Thermal management of batteries employing active temperature control and reciprocating cooling flow, International Journal of Heat and Mass Transfer. 83 (2015) 164–172.

https://doi.org/10.1016/j.ijheatmasstransfer.2014.11.079.

[24] D. Li, Z. He, C. Wang, S. Sun, K. Ma, Z. Xing, Simulation of dry screw vacuum pumps based on chamber model and thermal resistance network, Applied Thermal Engineering. 211 (2022) 118460. https://doi.org/10.1016/j.applthermaleng.2022.118460.

[25] D. Dan, W. Li, Y. Zhang, Y. Xie, A quasi-dynamic model and thermal analysis for vapor chambers with multiple heat sources based on thermal resistance network model, Case Studies in Thermal Engineering. 35 (2022) 102110. https://doi.org/10.1016/j.csite.2022.102110.

[26] J. Zhu, H. Zhang, G. Wu, S. Zhu, W. Liu, Thermal performance of cylindrical battery module with both axial and radial thermal paths: Numerical simulation and thermal resistance network analysis, Journal of Energy Storage. 49 (2022) 104197. https://doi.org/10.1016/j.est.2022.104197.

[27] S. Xu, Y. Wang, J. Shao, J. Li, Q. Yu, An electrochemical-thermal coupling model for prismatic lithium-ion batteries over wide temperature range, Applied Thermal Engineering. 217 (2022) 119282. https://doi.org/10.1016/j.applthermaleng.2022.119282.

[28] S.A. Asiri, E.M. Salilih, K.M. Alfawaz, A.F. Alogla, S.M. Sajadi, O.K. Nusier, Transient heat transfer analysis of serially connected array of phase change material in the thermal battery units with Al2O3 working Nano fluids, Journal of Energy Storage. 53 (2022) 105184. https://doi.org/10.1016/j.est.2022.105184.

[29] J. Chen, D. Ren, H. Hsu, L. Wang, X. He, C. Zhang, X. Feng, M. Ouyang, Investigating the thermal runaway features of lithium-ion batteries using a thermal resistance network model, Applied Energy. 295 (2021) 117038. https://doi.org/10.1016/j.apenergy.2021.117038.

[30] G. Wang, D. Kong, P. Ping, X. He, H. Lv, H. Zhao, W. Hong, Modeling venting behavior of lithium-ion batteries during thermal runaway propagation by coupling CFD and thermal resistance network, Applied Energy. 334 (2023) 120660. https://doi.org/10.1016/j.apenergy.2023.120660.

[31] X. Feng, L. Lu, M. Ouyang, J. Li, X. He, A 3D thermal runaway propagation model for a large format lithium ion battery module, Energy. 115 (2016) 194–208. https://doi.org/10.1016/j.energy.2016.08.094.

[32] DIN SPEC 91252 - Electrically propelled road vehicles - Battery systems - Dimensions for Lithium-Ion-Cells | GlobalSpec, (n.d.). https://standards.globalspec.com/std/1293452/DIN%20SPEC%2091252 (accessed February 17, 2023).